

# Imaging the Sun's Far-Side Active Regions by Applying Multiple Measurement Schemes on Multi-Skip Acoustic Waves

Junwei Zhao<sup>1</sup>, Dominick Hing<sup>2</sup>, Ruizhu Chen<sup>1</sup>, and Shea Hess Webber<sup>1</sup>

## ABSTRACT

Being able to image active regions on the Sun's far side is useful for modeling the global-scale magnetic field around the Sun, and for predicting the arrival of major active regions that rotate around the limb onto the near side. Helioseismic methods have already been developed to image the Sun's far-side active regions using near-side high-cadence Doppler-velocity observations; however, the existing methods primarily explore the 3-, 4-, and 5-skip helioseismic waves, leaving room for further improvement in the imaging quality by including waves with more multi-skip waves. Taking advantage of the facts that 6-skip waves have the same target-annuli geometry as 3- and 4-skip waves, and that 8-skip waves have the same target-annuli geometry as 4-skip waves, we further develop a time–distance helioseismic code to include a total of 14 sets of measurement schemes. We then apply the new code on the *SDO*/HMI-observed Dopplergrams, and find that the new code provides substantial improvements over the existing codes in mapping newly-emerged active regions and active regions near both far-side limbs. Comparing 3 months of far-side helioseismic images with the *STEREO*/EUVI-observed 304 Å images, we find that 97.3% of the helioseismically detected far-side active regions that are larger than a certain size correspond to an observed region with strong EUV brightening. The high reliability of the new imaging tool will potentially allow us to further calibrate the far-side helioseismic images into maps of magnetic flux.

*Subject headings:* Sun: helioseismology — Sun: oscillations — Sun: magnetic fields — sunspots — Sun: UV radiation

## 1. Introduction

The bulk of the Sun is not transparent to electromagnetic waves, thus active regions (ARs) on the Sun's far side are not directly visible to us; however, the Sun's helioseismic waves, mostly  $p$ -

---

<sup>1</sup>W. W. Hansen Experimental Physics Laboratory, Stanford University, Stanford, CA 94305-4085, USA

<sup>2</sup>Department of Physics, Stanford University, Stanford, CA 94305-4060, USA

mode (or acoustic) waves, can propagate through the Sun’s interior and bring far-side information to the near side. Most large far-side ARs are detectable through an analysis of such acoustic waves observed on the near side, and this allows us to monitor the evolution of large ARs throughout their lifetimes and to forecast arrivals of large ARs that rotate onto the Sun’s near side from its far side.

Lindsey & Braun (2000a) first detected a large AR on the Sun’s far side by employing helioseismic holography method (Lindsey & Braun 2000b) and using the Doppler-velocity data observed by the *Solar and Heliospheric Observatory /* Michelson Doppler Imager (*SOHO/MDI*; Scherrer et al. 1995). The far-side images from this first attempt, which utilized acoustic waves reflected twice on either side of the mapped far-side locations ( $2\times 2$ -scheme hereafter), are limited to only the central area within about  $50^\circ$  (here,  $^\circ$  represents heliographic degree) from the Sun’s far-side disk center. This limitation was later overcome by introducing a method that utilizes waves that are reflected once on one side and three times on the other side of far-side locations ( $1\times 3$ -scheme hereafter), and the entire far side was thus able to be mapped (Braun & Lindsey 2001). These helioseismic far-side maps, characterized by the phase shifts of helioseismic waves, are well correlated with the surface magnetic field and have a good potential to be calibrated into maps of unsigned magnetic flux (González Hernández et al. 2007).

Time–distance helioseismology (Duvall et al. 1993), another local helioseismic method, was also used to detect far-side ARs (Duvall et al. 2000). Later, Zhao (2007) more systematically developed this method to include both 4-skip (composed of both the  $2\times 2$ - and  $1\times 3$ -schemes) and 5-skip ( $2\times 3$ -scheme) acoustic signals, and the combination of both 4- and 5-skip waves helps to enhance the signal-to-noise ratio of the far-side images. Ionidis et al. (2009) demonstrated that 3-skip acoustic signals ( $1\times 2$ -scheme) can also be used in far-side imaging, the quality of which can be further improved by combining maps made from all of the 3-, 4-, and 5-skip helioseismic waves. All the above-mentioned measurement schemes are illustrated in Figure 1. Here, it is useful to caution that although both the helioseismic holography and time-distance methods employ  $2\times 2$ - and  $1\times 3$ -schemes, these two methods are fundamentally different in the measuring processes.

Prior to the availability of direct far-side observations, the reliability of imaging far-side ARs could only be assessed through applying the technique on numerical simulation data (Hartlep et al. 2008), or comparing the detected far-side ARs with the near-side ARs before their rotation onto the far side or after their rotation onto the near side. More recently, the validity of helioseismic far-side imaging can be better evaluated by comparing with the Sun’s far-side EUV observations of the Extreme UltraViolet Imager (EUVI) onboard the twin *Solar TERrestrial RELations Observatory (STEREO)* spacecraft (Howard et al. 2008). In a series of articles, Liewer et al. (2012, 2014, 2017) systematically compared *STEREO/EUVI* 304 Å images, in which ARs exhibit as regions of enhanced emission, with helioseismic holography far-side images made from observations of both *Global Oscillations Network Group (GONG)* (Harvey et al. 1996) and *Solar Dynamics Observatory*

/ Helioseismic and Magnetic Imager (*SDO/HMI*; Scherrer et al. 2012; Schou et al. 2012). They found that 95% of the helioseismically-detected far-side ARs correspond to an observed EUV brightening area, but only about 50% of EUV brightening areas correspond to a helioseismically detected AR. This gives us a sense of the reliability and limitation of the helioseismic holography far-side imaging method.

Imaging the Sun’s far-side ARs is useful for better space weather forecasting. Modeling coronal magnetic field and solar wind requires an input of global photospheric magnetic field, not just of the near side; however, the far-side magnetic field that is used in most models typically relies on observations of days earlier, or calculations from flux-transport models (e.g., Schrijver & DeRosa 2003; Upton & Hathaway 2014). Unfortunately, flux-transport models cannot model the ARs that continue to grow or that newly emerge on the far side, and this would cause inaccuracies in the far-side magnetic-field data used in the global field and solar wind modeling. The global magnetic field with updated far-side AR evolution, particularly for ARs that rapidly emerge and grow on the far side, is important for a more accurate modeling: e.g., Arge et al. (2013) applied their ADAPT model (Air-Force Data Assimilative Photospheric Flux Transport model; Arge et al. 2010) on an updated magnetic field map with a newly emerged far-side AR detected by the helioseismic imaging method, and found that their modeled solar wind result is in better agreement with the observation than the result without including the new far-side AR.

However, the reliability and quality of helioseismic far-side images still need to be improved for use in the forecasting models, and in fact can be improved. All the previous methods only explored the 3-, 4-, and 5-skip helioseismic waves, while waves with more skips are also useful but have not been explored in far-side imaging. In this article, taking advantage of the fact that 6-skip acoustic waves share the same surface target-annuli geometry with 3- and 4-skip waves, and that 8-skip waves share the same surface target-annuli geometry with 4-skip waves, we further implement the 6- and 8-skip waves in the existing time–distance far-side imaging codes and develop a new code. Through comparing the new far-side helioseismic images with images from the holography method, as well as with *STEREO*’s EUV 304 Å observations, we assess the reliability and the AR-detection success rate of the new far-side imaging code. The article is organized as follows: we introduce our new method development in Section 2, present new far-side imaging results in Section 3, and assess the reliability and success rate of the new imaging method in Sections 4 and 5, respectively. We then discuss our results and give conclusions in Section 6.

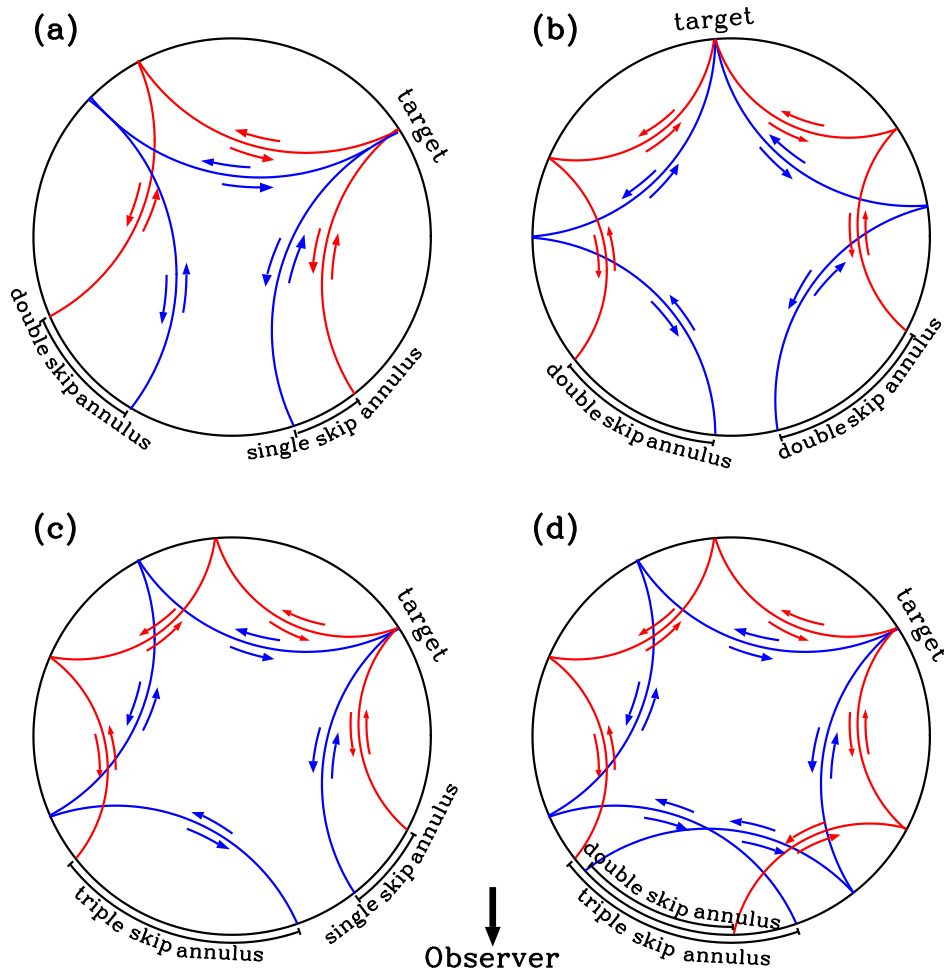


Fig. 1.— Measurement schemes, viewed as great-circle slices through far-side target points, for (a)  $1 \times 2$ -scheme for the sole branch of 3-skip waves; (b)  $2 \times 2$ -scheme for the lower branch of 4-skip waves; (c)  $1 \times 3$ -scheme for the lower branch of 4-skip waves; and (d)  $2 \times 3$ -scheme for the lower branch of 5-skip waves. With the observer situated toward the bottom of the page, the lower half of each circle represents the near side of the Sun, and the upper half the far side. In each scheme, red curves indicate the ray paths for the waves with the shortest travel distance that is used in the corresponding measurement scheme, and blue curves for the waves with the longest travel distance. The “target” marked on the far side represents a sample location to be mapped, and the annuli marked on the near side indicate the ranges, within which acoustic signals are taken for calculations.



## 2. Method

### 2.1. Multi-Skip Waves

As introduced in Section 1, the previous time–distance far-side imaging method used 3-, 4-, and 5-skip acoustic waves (Zhao 2007; Ilonidis et al. 2009). Starting from the near side, these waves experience a total of 3, 4, and 5 surface reflections during their travel to the far side and then back to the near side through the Sun’s interior. However, as shown in Figure 2, in the time–distance diagram obtained from 31-hr Doppler observations of *SDO/HMI*, not only the 3-, 4-, and 5-skip waves show clear signals, but the 6-, 7-, 8-, and 9-skip waves are also visible within the duration of 900-min wave travel time. The time–distance diagram is made through cross-correlating oscillatory signals between different surface locations, and is displayed as a function of time lag and great-circle distance,  $\Delta$ , between these surface locations, where the time lag in the cross-correlation functions is interpreted as travel time of acoustic waves from one surface location to the other. As can be seen in Figure 2, the correlation coefficients corresponding to the 6–9-skip waves, which is an indicator to the waves’ oscillatory amplitude, is not much lower than those corresponding to the 3–5-skip waves, demonstrating that waves experiencing more surface reflections do not decay much more and are suitable to be included in the far-side imaging computations. The waves experiencing more than 9 skips may still be strong and clean, but their longer travel times make them less practical to be used in the far-side imaging method, which typically uses observational data of 1 day or slightly longer.

The cross-correlation functions representing the 4- through the 9-skip waves (see Figure 2) exhibit a “<” shape with its left-most turning-point at the measurement distance  $\Delta = 0^\circ$ . Actually, the  $\Delta = 0^\circ$  for these signals that return from the far side represents a total of  $360^\circ$  travel distance around the globe, the lower branch of the “<” shape represents a travel distance of  $360^\circ - \Delta$ , and the upper branch represents a travel distance of  $360^\circ + \Delta$ . The waves in the upper branches have a slightly faster travel speed than those in the lower branches of the same skip, and travel a longer distance while experiencing a same number of surface reflections. They correspond to the oscillation modes with a lower harmonic degree  $\ell$ . The time–distance diagram in Figure 2 does not distinctly show the upper branch for the 3-skip waves, nor either branch of the 2-skip waves coming back from the far side, implying that these waves correspond to the low- $\ell$  modes that are either unresolvable in the *SDO/HMI* observations or do not possess a sufficiently high signal-to-noise ratio to show up in this 31-hr observation. It is worth pointing out that multi-skip acoustic waves traveling within the near side of the Sun can also be seen in Figure 2, but these waves are not useful in imaging the Sun’s far side. Shown as monotonically-upward ridges on the right side of the diagram, these waves can also be long-lasting, and many of them survive more than 20 surface reflections before completely decaying away.

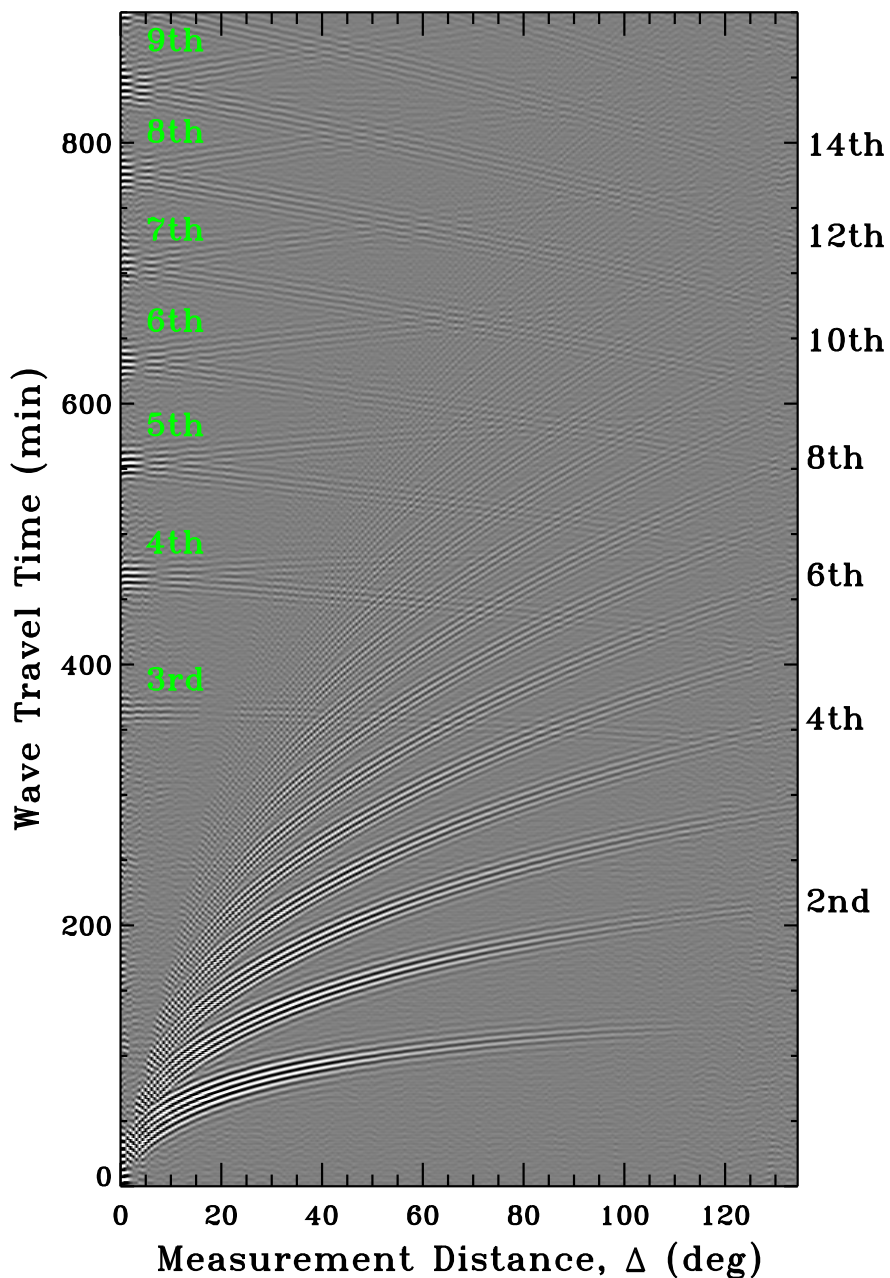


Fig. 2.— Time–distance diagram obtained from cross-correlating 31 hours of *SDO/HMI* Doppler-velocity data and displayed as a function of time lag (corresponding to wave travel time) and great-circle distance  $\Delta$  between the pairs used for the cross-correlation calculation. On the right-hand side of the axis mark the  $n$ -th skip of acoustic waves traveling within the near side of the Sun. Green letters near the left axis mark the  $n$ -th skip waves that arrive back to the near side after traveling to the far side and experiencing  $n$  surface reflections.

Zhao (2007) explored the lower branch of 4-skip waves and both branches of 5-skip waves, while Ilonidis et al. (2009) investigated the sole branch of 3-skip waves. This work further expands their analyses and includes the upper branch of 4-skip waves and both branches of the 6- and 8-skip waves in the new analysis method. This expansion takes advantage of the fact that measurements of 6-skip waves using a  $2 \times 4$ -scheme share the same surface target-annuli geometry as the  $1 \times 2$ -scheme for 3-skip waves, measurements of 6-skip waves using a  $3 \times 3$ -scheme share the same surface geometry as the  $2 \times 2$ -scheme for 4-skip waves, and measurements of 8-skip waves using  $2 \times 6$ - and  $4 \times 4$ -schemes share the same target-annuli geometries as the  $1 \times 3$ - and  $2 \times 2$ -schemes for 4-skip waves (see Figure 1). Although both 7- and 9-skip signals are expected to be useful in the far-side imaging, they are not included in our new code. No existing measurement scheme exists to accommodate the 7-skip waves; although the 9-skip waves can be used in a  $3 \times 6$ -scheme, same in surface geometry as the  $1 \times 2$ -scheme for 3-skip waves, the low imaging quality from the upper branch of 8-skip waves (see Sec. 3.2) demonstrates that the final far-side imaging quality may not benefit much from including the 9-skip waves.

## 2.2. Measurement Schemes

The basic method for imaging the Sun’s far-side ARs is described as follows. An acoustic wave starting from a near-side location expands like water ripples and seemingly sweeps across the whole Sun. Although the acoustic waves look much like surface ripples, they actually form so when acoustic waves travel into the interior and get refracted back continually from different depths of the solar interior. These ripples form the 1st-skip wave. The 2nd-, 3rd-, 4th-, ..., skip waves follow when the 1st-skip waves are reflected back into the interior and refracted again, and thus form a series of expanding ripples. Depending on their modes, some waves can travel very far and continue back to the original near-side location and even beyond after a few surface reflections, shown as left-side signals in Figure 2. The waves that get reflected inside a far-side AR experience a reduction in their total travel times, either because the wave speed is relatively faster beneath sunspots (Kosovichev et al. 2000; Hartlep et al. 2008), or due to plages around ARs (Lindsey & Braun 2017). Such a travel-time reduction can be measured using near-side observations to show the location, size, and perhaps magnetic-field strength of the far-side AR.

Because of significant fluctuations and uncertainties in the travel times measured from the waves traveling around the globe, it is unrealistic to obtain far-side AR information from measurements using merely one wave starting from one near-side location and ending at another near-side location. Instead, it is necessary to use all near-side locations that have a same great-circle distance (hereafter, distance means great-circle distance unless specified otherwise) to or from the far-side target, so that this far-side target effectively becomes a focus point where a great number

Table 1: Parameters for all the measurement schemes used in this study.

schemes <sup>a</sup>	annulus 1 range <sup>b</sup>	annulus 2 range <sup>b</sup>	covered range <sup>c</sup>
3-skip 1×2 lower <sup>†</sup>	96°5 – 108°5	193°0 – 217°0	18°4 – 77°6
4-skip 2×2 lower <sup>†</sup>	139°8 – 172°2	139°8 – 172°2	0°0 – 48°8
4-skip 2×2 upper	187°8 – 207°0	187°8 – 207°0	0°0 – 48°8
4-skip 1×3 lower <sup>†</sup>	69°3 – 85°5	207°9 – 256°5	46°4 – 90°0
4-skip 1×3 upper	93°5 – 105°5	280°5 – 316°5	71°2 – 90°0
5-skip 2×3 lower <sup>†</sup>	110°0 – 134°0	165°0 – 201°0	0°0 – 60°8
5-skip 2×3 upper <sup>†</sup>	150°0 – 175°2	225°0 – 262°8	0°0 – 76°0
6-skip 2×4 lower	99°5 – 110°3	119°0 – 220°6	16°8 – 80°0
6-skip 3×3 lower	147°0 – 171°0	147°0 – 171°0	0°0 – 48°8
6-skip 3×3 upper	189°0 – 219°0	189°0 – 219°0	0°0 – 48°8
8-skip 4×4 lower	153°0 – 171°0	153°0 – 171°0	0°0 – 48°8
8-skip 4×4 upper	187°8 – 215°4	187°8 – 215°4	0°0 – 48°8
8-skip 2×6 lower	73°5 – 94°5	220°5 – 283°5	42°4 – 90°0
8-skip 2×6 upper	93°5 – 102°5	280°5 – 307°5	62°4 – 90°0

<sup>a</sup>The “lower” or “upper” in each measurement scheme indicates that the lower or upper branch in the time–distance diagram is used in this scheme.

<sup>b</sup>Ranges for both annulus 1 and annulus 2 are great-circle distances from the far-side target.

<sup>c</sup>The distance range from the far-side disk center that can be covered by the corresponding measurement scheme.

<sup>†</sup>These measurement schemes were previously explored by Zhao (2007) and Ilonidis et al. (2009).

of waves get their surface reflections. Those near-side surface locations, one set as wave emitters and the other set as wave receivers, are pre-determined in order to save computational time in our calculation of the far-side images. In practice, a range of different travel distances are used for one measurement geometry. These locations form either an annulus or an arc segment in the near side of the Sun. Using 3-, 4-, and 5-skip waves as examples, Figure 1 displays our measurement geometries illustrated in a great-circle slice through a far-side target. Measurements using 6- and 8-skip waves have the same surface target-annuli geometries but different interior paths. Table 1 lists measurement parameters for all the 14 measurement schemes to be used in this work. All the numbers listed in the table are based on 0° solar  $B$ -angle. As a matter of fact, for the efficiency and simplicity of the computations, all the images are calculated for the far side of the apparent solar disk without considering the  $B$ -angle variations. The Carrington longitude and  $B$ -angle are only considered when remapping the far-side images into synchronic maps as shown in Sec. 4.

The measurement process is rather complicated, and we take the 1×3-scheme for the lower

branch of 4-skip waves (Figure 1c and Figure 3a) as one example to describe our measurement procedure. The single-skip annulus is taken as annulus 1 in Table 1, the triple-skip annulus is taken as annulus 2, and their corresponding measurement parameters are listed in Table 1 as well. As shown in Figure 1c, each annulus is delimited by a red curve and a blue curve, with the red curve representing the ray path for the acoustic waves with the shortest travel distance used in this measurement scheme, and the blue curve representing the waves with the longest travel distance. In most cases, although the “annulus” is not a complete annulus on the near side but a segment of the annulus, we still use the word “annulus” for simplicity of the description. This can be better seen in Figure 3b, which is plotted corresponding to Figure 3a but shows the locations of the annuli on the near-side solar disk from the observer’s point of view. The solar disk, plotted with a spatial resolution of  $0.6 \text{ pixel}^{-1}$  in the Postel-projected coordinates, is consistent with how the data are mapped and selected in our measurements. The locations inside annulus-segment “1a” represent pixels with the shortest 1-skip distance of  $69.3 - 69.9$  (with the annulus thickness of 1 pixel; and also refer to Table 1) away from the far-side target, which is at longitude of  $16.0$  past the west limb and latitude of  $21.1\text{N}$ , and the locations inside annulus-segment “2a” are pixels with the shortest 3-skip distances of  $206.1 - 207.9$  (with annulus thickness of 3 pixels) away from the far-side target. Annulus-segments “1a” and “2a” form a pair, inside which the Doppler-velocity signals are averaged respectively and then cross-correlated. Similarly, signals are averaged and cross-correlated for signals inside the pair “1b” and “2b”, which show locations of signals with the longest travel distance, as well as for all other pairs whose distances fall between these two shortest and longest pairs within the shaded areas of “1-skip annulus” and “3-skip annulus”. For each pair, the cross-correlation functions corresponding to both the positive time lags and negative lags are averaged to enhance the signal-to-noise ratio. In principle, the averaged cross-correlation functions represent, roughly, the waveform of waves traveling from one arc on the near side, through the Sun’s interior and far side, to the other arc on the near side. For one far-side target, multiple averaged cross-correlation functions can be obtained corresponding to the multiple wave-traveling distances, e.g., results from the pair 1a-2a and pair 1b-2b (Figure 3b) correspond to a same far-side target.

What is described above is only the measurement procedure for one single far-side target. Every different far-side target has different corresponding near-side annuli locations, and the same measurement procedure is repeated for each far-side target. For other measurement schemes shown in Figure 1a and 1d, a similar procedure is followed; however, the measurement procedure is slightly different for the measurement scheme shown in Figure 1b, in which the near-side locations usually form a complete annulus. For each travel distance in this scheme, we divide the whole annulus into four quadrant-annuli, inside each of which helioseismic signals are averaged and are cross-correlated with the averaged signals from the quadrant-annulus that is directly across.

The measurement schemes shown in Figure 1 and the measurement procedures described

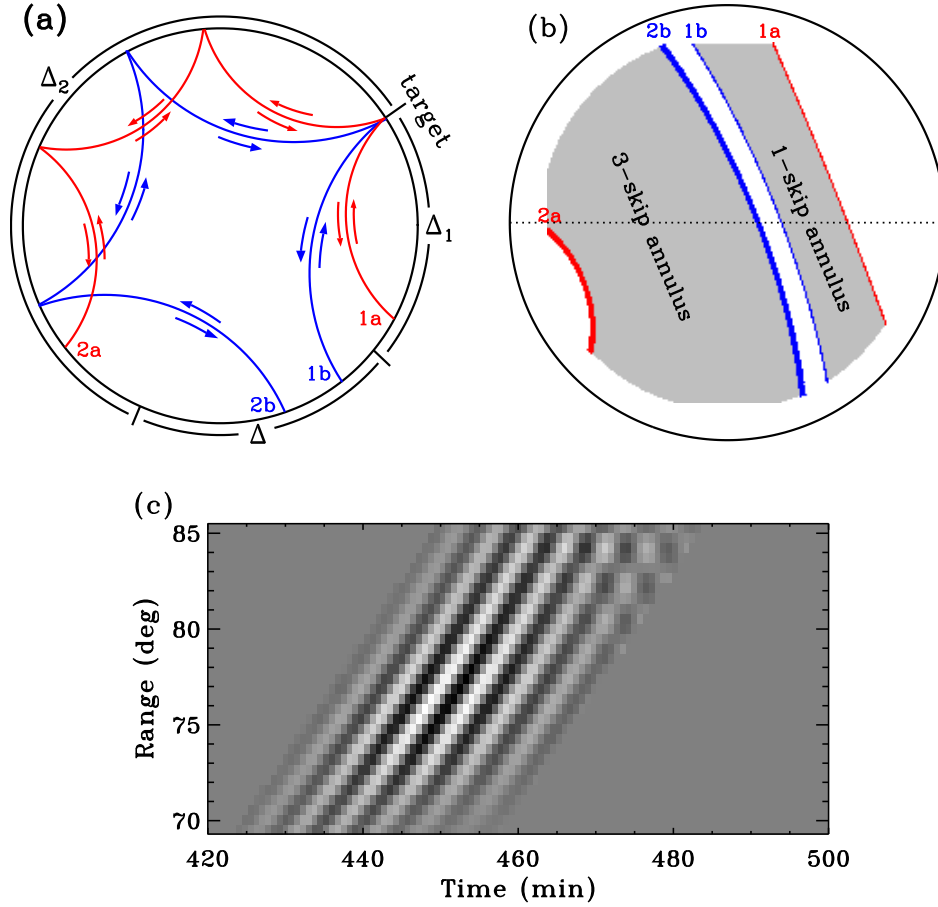


Fig. 3.— (a) Same as Figure 1c, but with “1a”, “1b”, “2a”, and “2b” marked corresponding to the annuli boundaries shown in panel b, and with distances  $\Delta$ ,  $\Delta_1$ , and  $\Delta_2$  marked. (b) Annuli locations on the near side of the Sun, displayed here in Postel’s projection with a  $0.6^\circ$  pixel size, for the measurement scheme shown in panel a. The far-side target is located at longitude of  $16^\circ 0'$  past the west limb and latitude of  $21.1^\circ \text{N}$ . Red annulus-segment 1a (blue annulus-segment 1b) indicates locations with the shortest (largest) 1-skip distance to the target, and red annulus-segment 2a (blue annulus-segment 2b) indicates locations with the shortest (longest) 3-skip distance to the target. Thickness of the annulus-segments indicate their widths. Shaded regions between 1a and 1b (2a and 2b) indicate the full range of 1-skip annuli (3-skip annuli) used in our calculation. Note that the annuli stop either at a distance of  $60^\circ$  away from the disk center or at the boundary of our datasets. (c) Reference time-distance diagram for the  $1 \times 3$ -scheme, obtained after a long-time average and to be used for deriving phase shifts for each far-side target. The vertical axis represents 1-skip distance range  $\Delta_1$ .

above are essentially the same as the method prescribed by Zhao (2007) and Ionidis et al. (2009).

Based on the existing code and the pre-determined near-side annuli locations corresponding to each far-side target location, we further expand the calculation to include more measurement schemes without significant changes to the existing code and the measurement strategy. As already pointed out in Section 2.1, measurement schemes for 6- and 8-skip waves, namely,  $2 \times 4$ -,  $3 \times 3$ -,  $2 \times 6$ -, and  $4 \times 4$ -schemes, are therefore adopted in our new code. Moreover, all waves that experience more than 3 skips have a lower branch and an upper branch, but double branches were only explored previously in the 5-skip waves; in this study, both branches are included in measurements for all the skips. Therefore, a total of 14 measurement schemes, as listed in Table 1, are utilized with only minor code-implementation efforts, resulting in a great expansion over the previous 5 schemes.

### 2.3. Deriving Phase Shifts

For each far-side target, with a location index  $(i, j)$ , and for each measurement scheme  $s$ , a series of cross-correlation functions  $\mathcal{C}_s^{i,j}(\tau, \Delta)$  are obtained as functions of travel-time lag  $\tau$  and near-surface measurement distance  $\Delta$ . As shown in Figure 3a,  $\Delta$  is related to  $\Delta_1$  and  $\Delta_2$ , the distances between the far-side target and the two separate annulus pairs, by  $\Delta = 360^\circ - (\Delta_1 + \Delta_2)$  for the lower-branch schemes and  $\Delta = (\Delta_1 + \Delta_2) - 360^\circ$  for the upper-branch schemes. The  $\Delta_1$  and  $\Delta_2$  are not independent of each other either, but are related by  $\frac{\Delta_1}{n_1} = \frac{\Delta_2}{n_2}$ , where  $n_1$  and  $n_2$  are the number of skips corresponding to the two annuli.

The functions  $\mathcal{C}_s^{i,j}(\tau, \Delta)$  look much like their respective lower or upper branch of the corresponding  $n$ th-skip ridge shown in Figure 2 or the example shown in Figure 3c. To derive the travel-time shift (or phase shift) caused primarily by the surface-focused far-side target, we take an approach different from the prior method (Zhao 2007). In the prior method, the cross-correlation function is shifted for each distance by an amount of time, determined from either a theoretical expectation or an empirical value measured from a long-time average, so that the cross-correlation functions at different distances are essentially in phase. Simply put, the wave patterns seen in Figure 3c are so shifted that they form a straight vertical pattern of black and white stripes. One final cross-correlation function, which results from averaging all the functions after the time shifting, is fitted using a Gabor wavelet function for the travel times. Now we adopt a different approach to measure the travel-time shifts, which is believed more accurate and more computationally efficient.

All cross-correlation functions  $\mathcal{C}_s^{i,j}(\tau, \Delta)$  for all far-side target locations for each measurement scheme covering a selected 3-month period (see Section 3.2) are obtained following the procedures described in Section 2.2. For each measurement scheme, we average all the available cross-correlation functions. These mean cross-correlation functions, which are less noisy and are essentially not shifted by surface magnetic field, are used as reference functions  $\mathcal{C}_s^{\text{ref}}(\tau, \Delta)$  for the following calculations. Figure 3c shows the reference cross-correlation function for the

4-skip  $1 \times 3$ -scheme lower-branch case. To calculate the phase shift for a far-side target, the cross-correlation function for this target at each distance is cross-correlated with the reference cross-correlation function for the same measurement distance, and this calculation is done in the Fourier domain with frequency dependence following the equation:

$$\delta\phi_s^{i,j}(\nu, \Delta) = \arg \left[ \mathcal{F}(\mathcal{C}_s^{i,j}(\tau, \Delta)) \cdot \mathcal{F}^\dagger(\mathcal{C}_s^{\text{ref}}(\tau, \Delta)) \right], \quad (1)$$

where symbol  $\mathcal{F}$  represents Fourier transform,  $\nu$  is frequency after the Fourier transform is applied on time  $\tau$ ,  $\dagger$  represents complex conjugate, and  $\arg$  takes the argument of the complex number. That is, the travel-time shift (phase shift) carried by a cross-correlation function is assessed through comparing with a reference function, a method recently explored and utilized by Chen & Zhao (2018) for a different study. In the Fourier domain, the relative phase-shift, which is the argument of the complex number, can be obtained for frequencies between 3.0 to 5.0 mHz. The phase shifts for multiple frequencies are averaged again for the phase shift corresponding to this far-side location and for this measurement distance. The same procedure is repeated for different measurement distances, and the mean phase-shift from all distances for this measurement scheme is then used as the relative phase-shift for this far-side target location, i.e.,

$$\delta\phi_s^{i,j} = \langle \langle \delta\phi_s^{i,j}(\nu, \Delta) \rangle_\nu \rangle_\Delta, \quad (2)$$

where  $\langle \rangle_\nu$  takes an averaging over all  $\nu$ 's, and  $\langle \rangle_\Delta$  averages over all  $\Delta$ 's. The above procedure is then repeated for all far-side locations (i, j) and repeated for all measurement schemes  $s$ . In the end, each measurement scheme gives one far-side map of acoustic phase shifts, although none of the measurement schemes (except the 5-skip  $2 \times 3$ -scheme) gives a map covering the entire far-side Sun.

### 3. Data Analysis and Results

#### 3.1. Data Preparation and Processing

Only low- and medium- $\ell$  helioseismic modes are needed for imaging the Sun's far-side ARs, therefore, the high-resolution Dopplergrams observed by *SDO/HMI* need to be pre-processed to reduce their spatial resolution before being used in our far-side imaging calculations. In our new code, we use the HMI vector-weighted data (data series “hmi.vw\_V\_45s” in the *SDO/JSOC* webpage; Larson & Schou 2018), which mimic *SOHO/MDI*'s structure program data (Kosovichev et al. 1997; Larson & Schou 2013) and have a pixel size of about  $0^\circ 60$ . The full-disk data of this type are tracked with the Carrington rotation rate and a temporal cadence of 45 sec, the same as the observational cadence. For the tracking, we select 00:00UT and 12:00UT of each day as the



middle time of a tracked period of 1860 min (31.0 hr), which is composed of 2480 *SDO/HMI* Dopplergrams. Each tracked full-disk Dopplergram is then converted to a Postel-projected map, with the apparent disk center at the middle time of the tracked period as the projected map center, so that the annual variation of the solar  $B$ -angle can be neglected in our calculation. The remapped image keeps a spatial resolution of  $0^{\circ}60 \text{ pixel}^{-1}$ . To examine the validity and robustness of using the vector-weighted low-resolution data as our data input, we have tested tracking, rebinning, and remapping HMI’s original data, and found that the full-resolution data give us essentially the same final far-side maps, but substantially slow down the processing.

As pointed out by Zhao (2007), to analyze the very weak signals of the waves that start from the near side of the Sun and end in the near side after traveling to the far side, filtering out high- $\ell$  modes is necessary to enhance the signal-to-noise ratio of the far-side maps. Generally, the acoustic modes covering a frequency range of 2.5 – 5.0 mHz and an  $\ell$  span of 3 – 50 are used, although the detailed filtering parameters slightly change from one measurement scheme to another, depending on the number of wave skips as well. This filtering process is done after Fourier transform is applied on our tracked datacube. Strictly speaking, using Fourier transform for filtering is not robust because distances between most locations are not precisely preserved in the Postel-projected maps; however, our test analysis using the spherical-harmonics-decomposed data showed that Fourier transform in this study is an acceptable compromise between quality and computation speed.

### 3.2. Far-Side Maps of Active Regions

Following the analysis procedure described in Section 2, we have processed 9-year-worth of *SDO/HMI* observations for the period of 2010 May 1 through 2019 July 31. In this study, we only choose the results of a 3-month period, covering 2014 January 1 to March 31, to examine the far-side imaging quality of our new code. For each of the tracked datacubes, a total of 14 far-side images are obtained, all of which (except the 5-skip  $2 \times 3$ -scheme that gives a full coverage) cover either the central part or both limb areas of the far-side Sun. Examining all images that are produced for the whole 3-month period, we find that it is unlikely that all the 14 far-side images can image the far-side ARs equally well for any given period. Some measurement schemes give systematically better imaging quality than other measurement schemes, but no specific measurement scheme can always map the far-side ARs better than all other schemes. However, it is true that our final far-side images, made from merging all the 14 measured images, possess consistently better quality than any images made from one single measurement scheme, and are nearly always better than the images made from our previous codes (Zhao 2007; Ilonidis et al. 2009).

The final far-side image is an average of all the 14 far-side images, with 12 of them having an

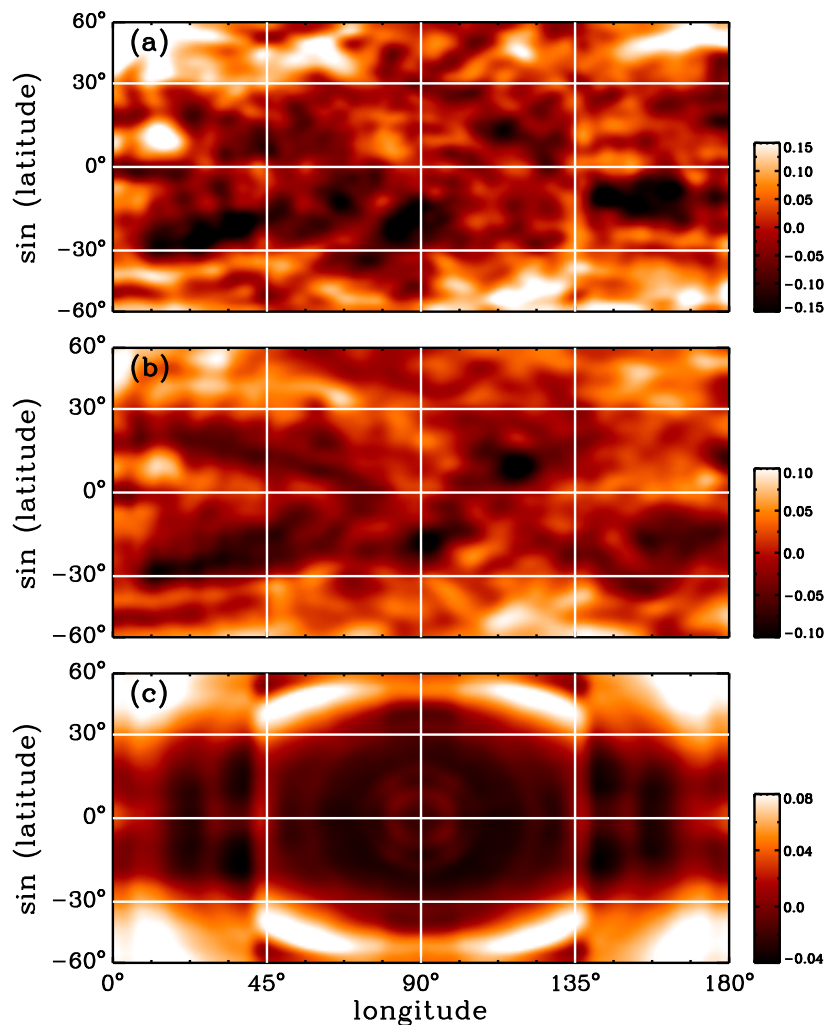


Fig. 4.— (a) Time–distance far-side image, obtained from a 31-hr period with a middle time of 00:00UT 2014 March 13, after averaging all available images that result from the 14 measurement schemes. (b) Far-side image after the image in panel (a) is overlapped and averaged with images of 3 prior days. (c) Background far-side image, averaged from all far-side images obtained during the analyzed 3-month period, but before the images are overlapped with images of prior days.

equal weight and the other 2, i.e., the schemes of “3-skip  $1 \times 2$  lower” and “8-skip  $2 \times 6$  upper”, assigned half weights of other schemes. These two schemes consistently give lower-quality images, and are hence assigned lower weights. Different areas of the far side are covered by a varying number of the 14 individual images, with a minimum coverage of 6 times close to the far-side limbs and a maximum of 14 times in the areas that join the central and limb regions around  $50^\circ$  from the far-side disk center. Other far-side areas receive a coverage of 8 times. Figure 4a shows an example of far-side images made over a 31-hr period centered at 00:00 UT, 2014 March 13.

Negative phase shifts (dark patches in the plot) are caused by the magnetic field of the far side, hence representing far-side ARs.

Despite the great improvement our new helioseismic far-side imaging code has made over the previous codes, it is also acknowledged that far-side images made from the 31-hr periods can only map the shape and size of far-side ARs very roughly. The shape and size of an AR can change significantly from one imaging period to the next, beyond the reasonable temporal evolution one would expect. To enhance the stability and reliability of their far-side images, Lindsey et al.<sup>1</sup> proposed to overlap one far-side image with the far-side images taken from 4 prior days (a total of 120 hours, or 5 days, of integration time), a process that sacrifices temporal resolution for image stability. In this study, we follow a similar approach but overlap one far-side image with the images obtained from 3 prior days (a total of 103 hours integration time considering each image is made from a 31-hr period), i.e., an average of 7 individual images after a uniform solar rotation (i.e., not differential rotation) is accounted for. However, not every far-side location has prior images to average with: the majority of far-side areas are averaged over 7 images, while the areas closer to the west limb are averaged fewer times. Figure 4b shows an example far-side image, obtained after the image in Figure 4a is averaged with images of 3 prior days; Figure 5b shows the same image in a different coordinate system. The overall shape, size, and strength (i.e., the amount of helioseismic-wave phase-shifts) of most ARs get altered after such averaging, but these ARs and their physical parameters become more consistent and stable from day to day, allowing us to potentially calibrate the far-side helioseismic maps into magnetic flux maps in the future.

Figure 4b and 5b are displayed with a scale of  $-0.10$  to  $0.10$  radians in the measured phase shifts, which correspond to a travel-time shifts of about  $-5.3$  to  $5.3$  sec. This display scale is selected arbitrarily, which unavoidably impacts how the far-side images of ARs are perceived in their size and strength. However, the selection of this display scale allows a better match, albeit only visually, of the helioseismic far-side ARs with the *STEREO*/EUVI 304 Å images of ARs (see Section 4).

We also acknowledge that despite our new efforts, artifacts still remain in the new far-side maps of ARs. Figure 4c shows a background image, obtained after averaging all the far-side images of the three analyzed months of 2014 before the images are shifted and overlapped for a more stable image quality. As already mentioned, phase shifts obtained at different far-side locations result from different measurement schemes using acoustic signals of slightly different wave modes observed at different near-side locations; therefore, it is not surprising that the phase shifts vary with far-side disk location in addition to the AR-caused shifts. Generally, the phase shifts tend to be smaller in low-latitude areas and larger in the near-limb and higher-latitude areas,

---

<sup>1</sup><http://jsoc.stanford.edu/data/farside/>

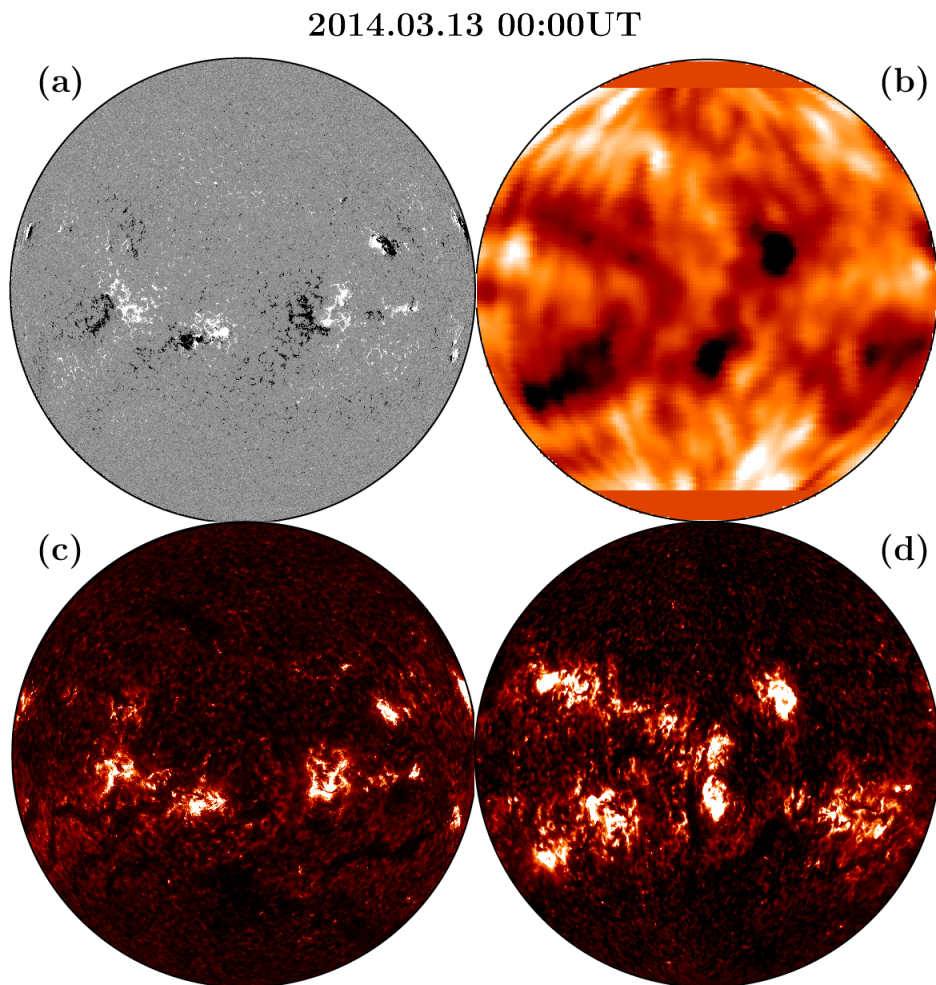


Fig. 5.— Comparison of near-side and far-side images taken at or near 00:00 UT of 2014 March 13. (a) *SDO/HMI*-observed near-side magnetic field; (b) helioseismic far-side image, same as Figure 4b but displayed in a different coordinate frame; (c) *SDO/AIA*-observed near-side 304 Å image; (d) *STEREO/EUVI*-observed far-side 304 Å image after merging observations from both *STEREO-A* and *STEREO-B* spacecraft. The magnetic field is displayed with a scale of  $-200$  to  $200$  Gauss, the helioseismic image is displayed with a scale of phase shifts from  $-0.10$  to  $0.10$ , and the EUV images are displayed with a DSN from 10 to 2000. The *STEREO/EUVI* 304 Å image is displayed after its intensity is calibrated to match the *SDO/AIA* 304 Å level.

where white (positive) patches appear. This is likely due to the near-side systematic center-to-limb effect in helioseismic measurements (Zhao et al. 2012) leaking into the far-side images. It is not straightforward to remove this effect, at least not by simply subtracting this mean background image from every far-side image, because this would cause artificial ARs near the limb and high-latitude areas in many far-side images. Fortunately, only dark patches corresponding to negative

phase shifts are useful in identifying far-side ARs, and those white patches can be neglected for the time being.

## 4. Comparisons

### 4.1. Comparisons with *STEREO* Far-Side EUV Images

As introduced in Section 1, two *STEREO* spacecraft together monitored the Sun’s entire far-side activity during February 2011 and October 2014. Particularly, the 304 Å images observed by *STEREO*/EUVI are highly correlated with maps of magnetic flux (Ugarte-Urra et al. 2015), giving us valuable pictures of the far-side ARs that can be used to assess the reliability of helioseismic far-side imaging techniques (Liewer et al. 2017). Figure 5 shows a comparison of the Sun’s *SDO*/HMI-observed near-side magnetic field and *SDO*/AIA-observed EUV 304 Å flux, together with a far-side helioseismic image from our new method and *STEREO*/EUVI-observed 304 Å image, all taken at about a similar time 00:00UT of 2014 March 13 (keep in mind that the helioseismic image results from a 103-hr average).

The comparison of Figure 5a and 5c shows the good correlation between the ARs’ magnetic flux and their 304 Å brightness enhancements, implying that the areas of 304 Å brightening can be used as a good indicator to the locations and sizes of ARs. The comparison between Figure 5b and 5d is a representation of how the far-side helioseismic images are comparable with the 304 Å images of ARs. It can be seen that the helioseismic method is capable of mapping most of the major ARs, with a good location and size indication, but loses detailed structures of these regions due to the poor spatial resolution resulting from the long helioseismic wavelengths used in our method. It is likely that the phase shifts measured in these far-side ARs and the EUV 304 Å flux density observed for the same ARs have a good correlation, but this needs further confirmation. Overall, Figure 5 demonstrates a promising potential that the far-side helioseismic images can be calibrated into far-side magnetic-flux maps by using the *STEREO*’s 304 Å images as a stepping-stone.

### 4.2. Comparisons with Helioseismic Holography Far-Side Images

Including more time–distance helioseismic measurement schemes unsurprisingly gives us better far-side imaging quality than the previous time–distance far-side imaging method (Zhao 2007; Ilonidis et al. 2009). Meanwhile, it is also desirable to compare our new results with the routine *SDO*/JSOC far-side images produced by the helioseismic holography method, which has also been upgraded in recent years to better accommodate the *SDO*/HMI data as well as to improve the

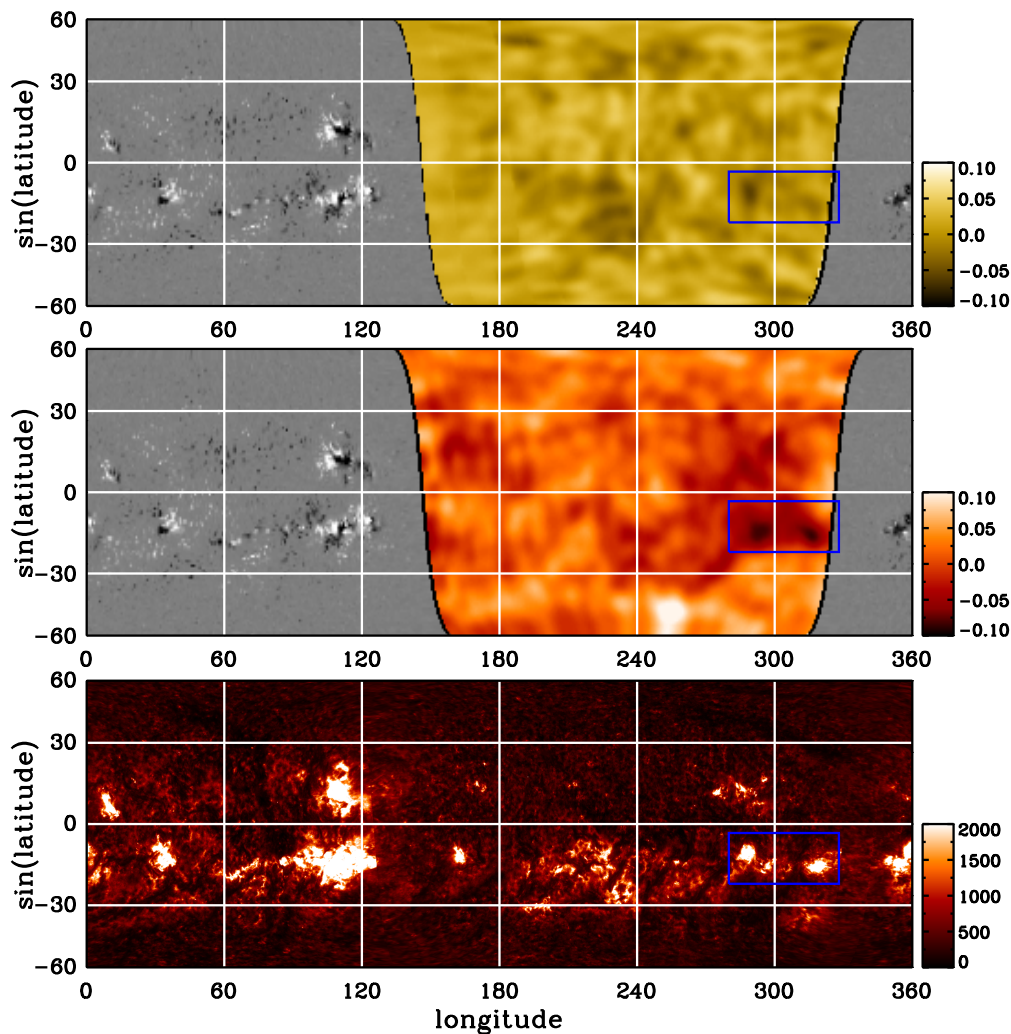


Fig. 6.— Comparison of the helioseismic holography far-side image, our new time–distance far-side image, and the EUV images taken at 12:00UT, 2014 February 7. Top panel shows a synchronic chart of *SDO/JSOC* helioseismic holography far-side image (*color*) and *SDO/HMI* near-side magnetic field (*black and white*); middle panel is a similar chart composed of time–distance far-side image (*color*) and near-side magnetic field; and bottom panel shows a combination of simultaneous 304 Å observations of *SDO/AIA* and both *STEREO* spacecraft. All images are mapped into the same Carrington longitude –  $\sin(\text{latitude})$  coordinates, and only latitudes between  $-60^\circ$  and  $60^\circ$  are displayed. Magnetic field is displayed with a range of  $-200$  to  $200$  Gauss. Areas delimited in the blue boxes are chosen for comparisons.

imaging quality. Figures 6 – 8 show a few representative comparisons of the images from the two helioseismic methods and the corresponding *SDO/AIA* and *STEREO/EUVI* images, highlighting a few selected ARs: near the east limb not long before they rotate onto the near side, near the west



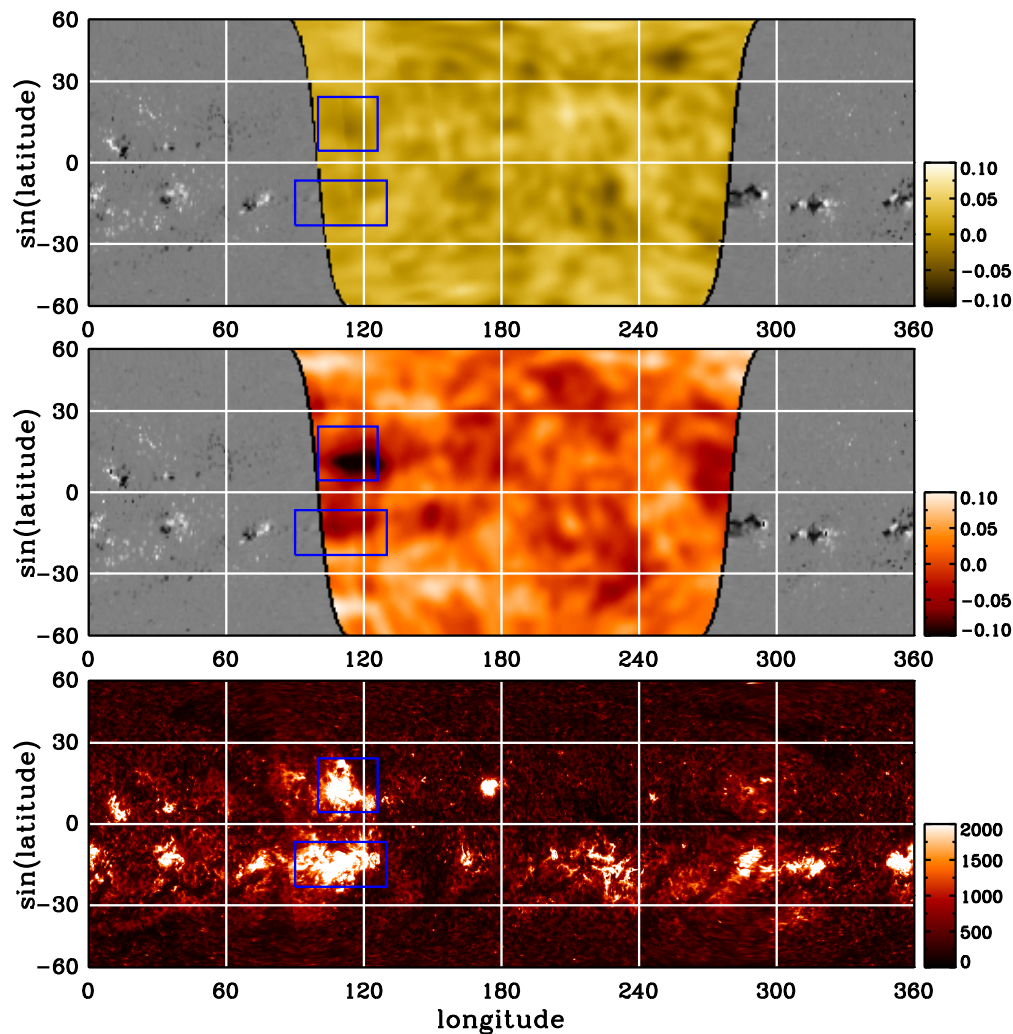


Fig. 7.— Same as Figure 6, but for 00:00UT, 2014 February 11.

limb not long after they rotate onto the far side, and not long after a far-side AR emergence. In these figures, the data for both the helioseismic holography images and magnetic fields are downloaded from *SDO/ISOC* website, and the data for the composite 304 Å images were prepared by Liewer et al. (2017) and kindly provided to us by the authors.

The capability of predicting arrivals of large ARs, which rotate into the Earth’s view from the Sun’s east limb, is practically useful for space weather forecasting. Figure 6 highlights two ARs, delimited in the blue box, about 1 day before they appeared on the near side. These two ARs would become NOAA AR11976 and AR11977 after their near-side appearance. Both the helioseismic holography and time–distance images are displayed with a same scale of  $-0.10$  to  $0.10$  phase-shift, which is consistent with the display scale of the online holography images at the

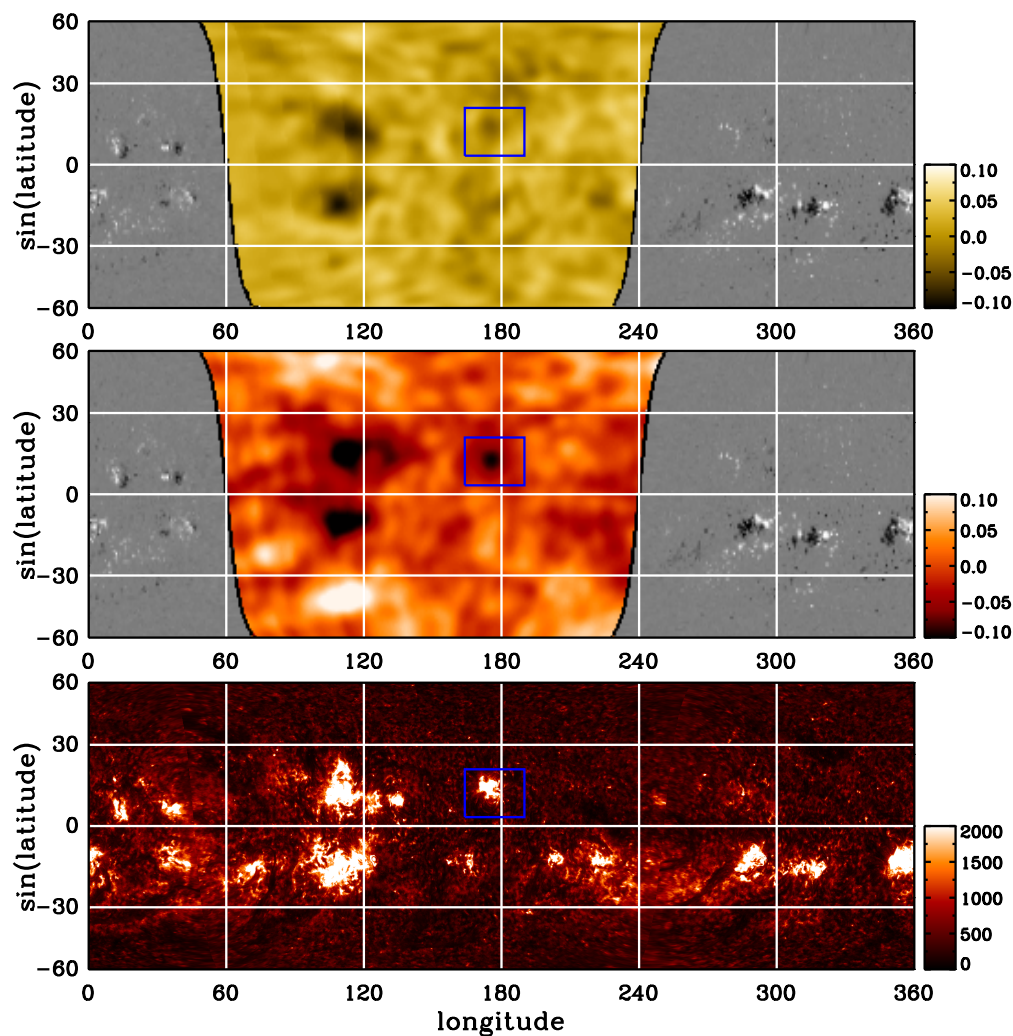


Fig. 8.— Same as Figure 6, but for 00:00UT, 2014 February 14.

*SDO/JSOC* website. It can be seen that the time–distance image unambiguously detects the two highlighted ARs, which approximately agree in location with the brightening areas (presumably ARs) observed in  $304 \text{ \AA}$ . The location difference between the time–distance helioseismic images and the  $304 \text{ \AA}$  observations falls within the spatial uncertainties of the helioseismic images, which can be as poor as  $10^\circ$ . That the helioseismic holography fails to show these ARs is not due to the display scale of the image, because the signals inside the blue box do not exceed the variation level of the background.

Figure 7 shows an example of two other ARs, AR11967 in the southern hemisphere and AR11968 in the northern hemisphere, about 1 day after their rotation from the Sun’s west limb onto the far side. As pointed out in Section 3, both the holography and time–distance methods show the



far-side near-west-limb areas with fewer days’ image overlapping, unlike most other areas on the far side. It is therefore expected that ARs in this area are not as reliably mapped. Nevertheless, the time–distance method shows one of the two ARs (the upper one) unambiguously, whereas the holography method does not show either AR convincingly.

Other than the ARs near both the far-side limbs, both helioseismic holography and time–distance methods give essentially consistent results in most areas of the far side, except for emerging ARs. Undoubtedly, new ARs also emerge on the far side, and some of them emerge rapidly and become strong and large enough to be detectable through helioseismic methods not long after their emergence. Figure 8 shows such an example. According to the *STEREO* observations that do not require a days-long integration like the helioseismic methods, the magnetic flux emergence started before February 11, when it is already visible in the 304 Å map in Figure 7, but only became unambiguously visible in the time–distance far-side images 3 days later on February 14. The holography method picks up the signal of this region unambiguously two more days later on February 16. The reason that the time–distance method only detects this emerging region over 3 days after its emergence is two-fold: first, as will be discussed in more detail in Section 5, helioseismic methods are only sensitive to the ARs that are larger than a certain surface area and stronger than a certain magnetic-field strength; second, averaging with 3-day prior images smears temporal resolution of the helioseismic images. It is possible that our method detects this emerging region 1 or 2 days earlier, but the region becomes ambiguous after averaging with earlier images that do not detect this AR.

These above examples demonstrate that our new far-side imaging code has an advantage over the helioseismic holography method in the detection of newly emerged ARs and ARs near both the far-side limbs.

### 4.3. Synoptic Far-Side Maps

Rather than selected snapshots with only one or two ARs, which may happen to be well or badly mapped, a Carrington synoptic map made from one entire rotation of the Sun can give us a more general perception of the reliability of the helioseismic far-side images. Figure 9 shows a comparison of a couple of pairs of synoptic maps made from far-side helioseismic images and *STEREO* 304 Å images. One pair of the data, shown in Figure 9a and 9b, from the helioseismic and the EUV images, respectively, are made by overlapping 30°-wide longitudinal bands across the far-side central meridian using two images per day; and another pair, shown in Figure 9d and 9e, are made by overlapping 30°-wide bands across the 60° longitude east of the far-side central meridian. Figure 9 also includes two near-side synoptic maps of magnetic field, obtained from 30°-wide bands across the near-side central meridian for the Carrington rotation before the same

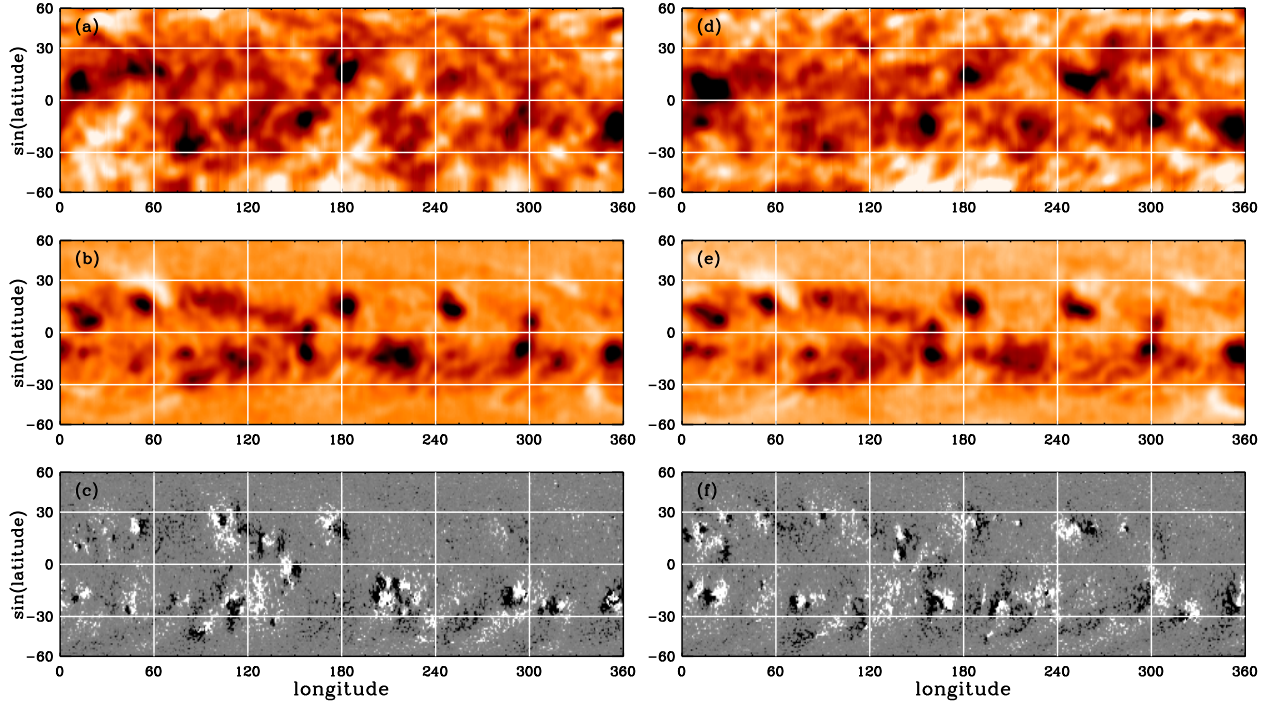


Fig. 9.— Synoptic maps of (a) time–distance helioseismic phase shifts using data near the far-side central meridian, (b) *STEREO*/EUVI 304 Å flux using the data near the far-side central meridian, displayed in the negative of the logarithm of the flux, (c) near-side magnetic field of Carrington rotation (CR) 2147. (d–e) Same as panels (a–b), but made using the data 60° east of the far-side central meridian. (f) Same as panel (c) but for CR2148. Panels (a) and (b) use the data of 2014 February 26 through March 23, and panels (d) and (e) use the data of March 2 through 27. CR2147 covers the period between February 11 and March 10, and CR2148 covers March 10 through April 6. The far-side helioseismic maps are displayed with a range of  $-0.08$  to  $0.06$ , the far-side EUV images are displayed with a range of  $-7.5$  to  $-5.0$ , and magnetic field charts are displayed with a range of  $-100$  to  $100$  Gauss.

regions rotate onto the far side and after they rotate out of the far side. That is, one set of the far-side synoptic maps is made half of a rotation after the same areas are used to make the first near-side synoptic magnetic map, and another set just 30° before they rotate back into the near side. It is worth pointing out that the central area of the helioseismic far-side images primarily result from the 4-skip  $2 \times 2$ , 6-skip  $3 \times 3$ , and 8-skip  $4 \times 4$  measurements schemes, and the limb areas are primarily made using other measurement schemes; therefore, these two sets of synoptic maps (Figure 9a and 9b) essentially show us the sensitivity and reliability of different schemes.

Comparing Figure 9a and 9b, and Figure 9d and 9e, we find that many ARs from the helioseismic images and the EUV maps agree with each other, although the size, shape, and exact location

differ in most cases. However, there are a couple of clear exceptions at coordinates of approximately  $(210^\circ, -15^\circ)$  and  $(250^\circ, 10^\circ)$ , where the helioseismic ARs are largely missing in Figure 9a. However, if we refer again to Figure 9d that is made with different measurement schemes using the data of about 5 days later, we find that the region at  $(250^\circ, 10^\circ)$  is actually a new emerging region that was still growing when the data for Figure 9a were taken. The region at  $(210^\circ, -10^\circ)$  is just the opposite, fast decaying when it was near the central meridian based on the EUV map. However, despite its weakened strength, it becomes detectable in Figure 9d, implying that weaker ARs are easier to be detected closer to the east limb than in other far-side locations. This is very useful because ARs closer to the east limb are more likely to cause space-weather effects as they rotate toward the near side.

We again caution that only negative phase shifts in the helioseismic far-side maps are meaningful in identifying and possibly calibrating ARs, and the positive patches in such maps are mostly due to the systematic center-to-limb effect in our local helioseismology technique, hence cannot be interpreted as AR-related or other surface- or interior-related features.

## 5. Success Rate

In Section 4, through comparing far-side images obtained from our new helioseismic code with the *STEREO*/EUVI observations of  $304 \text{ \AA}$  flux, we see how helioseismic images of ARs agree or disagree with the EUV brightening areas of ARs. However, a statistical assessment of success rate of our new helioseismic detection, just as what Liewer et al. (2014, 2017) have done for the helioseismic holography far-side images, is necessary. Here, we use the same 3-month period of helioseismic data used in Sections 3 and 4, and the contemporaneous composite  $304 \text{ \AA}$  maps as shown in Figures 6 – 8 for such a statistical assessment.

### 5.1. Data Preparation

Each of our helioseismic far-side images has only  $225 \times 121$  pixels, covering  $180^\circ$  in longitude and  $120^\circ$  in latitude (we use  $\sin(\text{latitude})$  in calculation, though), and each snapshot image results from an average of 103-hr observations. Therefore, for a fair and reasonable assessment of helioseismic images against the  $304 \text{ \AA}$  observations, two steps need to be taken: first, lower the spatial resolution of the  $304 \text{ \AA}$  images to match that of the helioseismic images; and second, average the  $304 \text{ \AA}$  images with the images of prior days in the same way the helioseismic images are averaged.

The composite  $304 \text{ \AA}$  maps, prepared and provided to us by Liewer et al. (2017), cover the

entire Sun with  $3600 \times 1800$  pixels and are in longitude – latitude coordinate. We first take a logarithm of the EUV flux values, so that small areas of high flux density do not spread to larger areas in the process of reducing the spatial resolution. Then we reduce the spatial resolution by convolving each EUV image with a two-dimensional Gaussian function that has a FWHM of  $4.71^\circ$ . The selection of the width of the Gaussian function is empirical: we tested a number of different FWHM parameters and selected the one that best visually matches the helioseismic images. However, we also acknowledge that given the apparent differences between the EUV images and helioseismic images, as can be seen in Figures 5-9, the “best match” is poorly defined.

The spatially-reduced EUV images are then remapped from the longitude – latitude coordinates to longitude –  $\sin(\text{latitude})$  coordinates to match the helioseismic images through bilinear interpolation. The Carrington longitude covers  $180^\circ$  (more or less, depending on the solar  $B$ -angle) of the far side; only observations between  $-60^\circ$  and  $60^\circ$  latitude are kept for further analysis, because no ARs appear higher than latitudes of  $60^\circ$ . The EUV images are then rebinned to the same number of pixels of the helioseismic images, each pixel having a size of  $0.8^\circ \times 0.8^\circ$ , or 0.64 square degrees (the degree and square degree correspond to the pixel sizes at the disk center). Such pixels, each equivalent to approximately  $31.0 \mu\text{hemispheres}$ , will be referred as helioseismic-image pixels (HIPs) hereafter.

To match the temporal averaging of the helioseismic images, each EUV image is overlapped and averaged with images of 3 prior days, using two images of 12-hr apart each day. Thus, the final resultant EUV images have both spatial and temporal resolutions matching those of the helioseismic far-side images, and these two types of images can then be overlapped for a comparative statistical analysis.

## 5.2. Matching Criterion

There are a total of 180 far-side helioseismic images, and the same number of EUV images, during the studied three months. Each helioseismic and EUV far-side image, despite resulting from 103-hr and 3.5-day average, respectively, is considered a random snapshot of the Sun’s far side and compared individually. That is, unlike the approach of tracking one AR across the far-side disk (Liewer et al. 2017), we consider an AR in one snapshot as one individual AR, although the same AR almost certainly appear on the following images. This way, many successfully-detected ARs are counted multiple times, and meanwhile, those undetected ARs may also be counted as failures multiple times. This may seem to cause biased results; however, because any individual image can be thought as a snapshot from a random day, there are a sufficient number of ARs through the 90-day period to make the statistics unbiased. Also, a single AR may not be successfully detected throughout its lifetime on the far side, as seen in Figure 9, so this approach helps take into account

the number of sporadic failed detections which would otherwise be considered complete failures.

None of the far-side ARs have a NOAA-denominated active region number, thus the boundaries of these ARs are not defined. After the reduction of the EUV flux maps' spatial resolution, it is possible that two or more adjacent ARs cannot be clearly distinguished with a distinct separation. In such a case, we count the ARs as one in this study. After convolving with the Gaussian function, the areas of EUV ARs become substantially larger and boundaries become more blurred. Therefore, it is highly likely one AR in our counting is composed of more than one AR based on the NOAA definition.

Some regions are too small in areas or too weak in EUV flux to be detectable in the helioseismic far-side images, so it is meaningful to only count and compare the regions exceeding both a certain area in size and a certain value in EUV flux density. Note that such small ARs may not cause a significant space weather concern, or cause a meaningful change in the large-scale magnetic field configuration. In this statistical study, we count the areas that have a logarithm value greater than 7.0 as the areas of the AR, and only those regions with a total area greater than 10 HIPs are counted as ARs in the following analysis. For the helioseismic images, we count the areas with a magnitude of phase shift greater than 0.06 radians, and again only those regions with a total area greater than 10 HIPs are counted as one AR in the statistical study. The selections of 7.0 as an EUV flux criterion, 0.06 as a helioseismic phase-shift criterion, and 10 HIPs as the minimum area for an AR are rather arbitrary, but as we can see in our later analysis, these selection criteria can only affect the success rate for the lower end of the statistics, but have little impact on large ARs.

We plot the EUV flux maps on top of the contemporaneous helioseismic images, and identify the regions that are counted as ARs in both types of maps based on the criteria given above. Understandably, helioseismic imaging cannot give a precise location for ARs due to its limit in spatial and temporal resolution, thus ARs that are identified as a positive match in EUV and helioseismic images may not entirely overlap each other. In practice, if an EUV AR overlaps with a helioseismic AR in 10 or more HIPs, we count them as a match. It is also found true that a large EUV AR may only correspond to a small helioseismic AR, or vice versa; we still count them as a positive match as long as they have 10 or more HIPs overlapping each other regardless of their respective sizes.

### **5.3. Success Rate**

It is not surprising that the AR-detection success rate of helioseismic imaging depends on the AR sizes. We have identified a total of 1022 ARs in the 90-day EUV maps, and a total of 777 ARs in the helioseismic images during the same period. Note that many of these ARs are not independent ARs, because we do not follow ARs but treat every single far-side image as a random

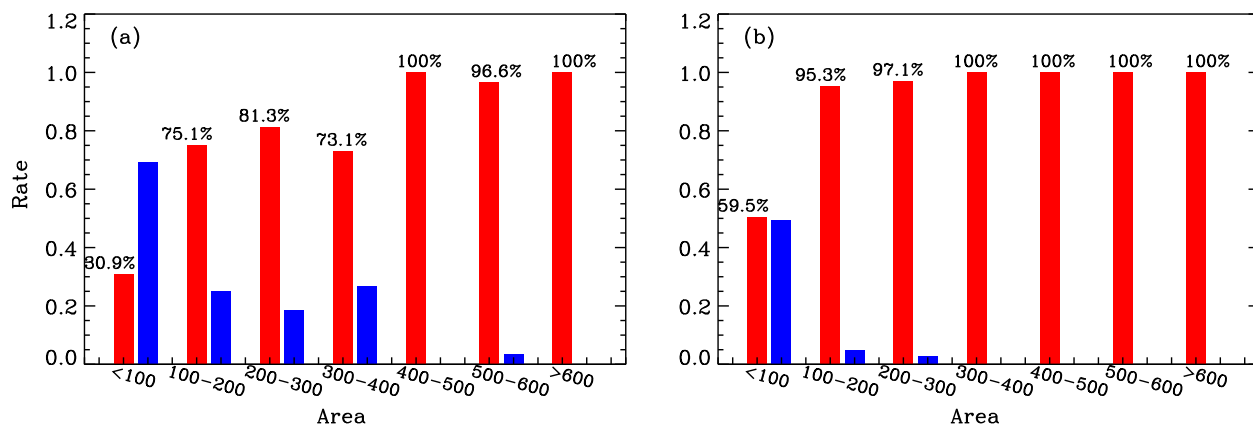


Fig. 10.— (a) Percentage of EUV ARs that correspond to (red) or fail to correspond to (blue) a helioseismic AR. (b) Percentage of helioseismic ARs that correspond to (red) or fail to correspond to (blue) an EUV AR. The percentages are categorized based on the areas of EUV ARs (a) and helioseismic ARs (b), which are plotted as horizontal axes with units of HIPs.

snapshot of the far side.

To break down the numbers, for the EUV-identified ARs, of the 512 ARs with a size between 10 and 100 HIPs, 158 (30.9%) correspond to an AR detected in the helioseismic images; of the 287 EUV ARs with a size of 100 – 200 HIPs, 211 (75.1%) correspond to an AR in the helioseismic images; of the 91 EUV ARs with a size of 200 – 300 HIPs, 74 (81.3%) correspond to an AR in the helioseismic images; of the 52 EUV ARs with a size of 300 – 400 HIPs, 38 (73.1%) correspond to an AR in the helioseismic images; of the 25 EUV ARs with a size of 400 – 500 HIPs, all (100%) of them correspond to an AR in the helioseismic images; of the 29 EUV ARs with a size of 500 – 600 HIPs, 28 (96.6%) correspond to an AR in the helioseismic images; of the 26 EUV ARs with a size greater than 600 HIPs, all (100%) correspond to an AR in the helioseismic images. A histogram of this statistic is shown in Figure 10a.

From the other perspective, of the 418 helioseismically-detected ARs that have a size between 10 and 100 HIPs, 211 (50.5%) correspond to an EUV-observed AR; of the 149 helioseismic ARs with a size of 100 – 200 HIPs, 142 (95.3%) correspond to an EUV AR; of the 68 helioseismic ARs with a size of 200 – 300 HIPs, 66 (97.1%) correspond to an EUV AR; of the 59 helioseismic ARs with a size of 300 – 400 HIPs, 27 helioseismic ARs with a size of 400 – 500 HIPs, 25 helioseismic ARs with a size of 400 – 500 HIPs, and 30 helioseismic ARs with a size greater than 600 HIPs, all (100%) of them correspond to an EUV AR. A histogram of this statistic is shown in Figure 10b.

Overall, 85.7% of all EUV ARs with a size larger than 200 HIPs are detected by the helioseismic imaging technique, and nearly 100% of the ARs larger than 400 HIPs are detected helioseismically. Even better, almost all (97.3%) of the helioseismic-identified ARs with an area greater

than 100 HIPs, correspond to an observed EUV AR. This indicates that not all of the far-side ARs can be detected helioseismically, but the helioseismically detected regions, as long as their sizes are greater than a certain size, almost all correspond to a true far-side AR.

## 6. Discussion and Conclusion

Both the helioseismic holography and time–distance helioseismic methods for imaging the Sun’s far-side active regions have existed for many years. In this paper, building upon existing time–distance far-side imaging codes and expanding the number of measurement schemes from the previous 5 to the current 14 (see Table 1), we have demonstrated that including more measurement schemes and using waves with a higher number of surface reflections substantially enhance the reliability and stability of far-side AR images.

Through comparing our new far-side images with the existing far-side images made from the helioseismic holography technique, we find that the new method has a substantially better sensitivity in detecting ARs near both the far-side limbs. Particularly, a successful detection of ARs near the east limb, one or two days before their appearance on the near side of the Sun, is very useful for predicting the arrival of major ARs, hence improved space weather forecasting. We also find that our new method has an advantage over the holography method in earlier detection of newly emerged ARs on the far side. Because the emergence of a large AR can significantly alter the global-scale magnetic field configuration, the information on the new emergence is important to the global-scale modeling of the Sun’s coronal magnetic-field structure and to modeling the solar wind. The helioseismic holography method uses a 5-day average to improve the stability of maps while our method uses 4-day averages, and this plays a role in the later detection of new emerging regions by the holography method. However, on the other hand, improving the stability of maps through overlapping a shorter period of data is itself an improvement. We also acknowledge that the holography method does a better job than our new method in ridding the systematic effects (positive patches) in high-latitude areas.

By comparing our new far-side images with *STEREO*/EUVI 304 Å observations, we find that our new method is capable of detecting the majority of far-side ARs of medium and large size, with a good approximation in size, location, and strength; however, only the ARs larger than a certain size and stronger than a certain flux threshold are reliably detected by the helioseismic imaging method. Our statistics shows that about 85.7% of ARs observed by *STEREO* with a size larger than 200 HIPs are detectable in the helioseismic images, while nearly all the helioseismically-detected ARs with an area larger than 100 HIPs correspond to an AR observed by *STEREO*. Therefore, every helioseismically-detected AR, as long as its size is greater than 100 HIPs, corresponds to an AR with very few number of false positive alarms. However, we need to caution that the area sizes

given here are after the original *STEREO* 304 Å images are convolved with a Gaussian function, hence substantially larger than the true sizes of those ARs.

A comparison of helioseismic far-side images with the *STEREO*-observed 304 Å images, and a comparison of the *SDO/HMI*-observed magnetic-field maps and the *SDO/AIA*-observed EUV images, together demonstrate that the helioseismic far-side images have a great potential to be calibrated into far-side maps of magnetic flux by using the 304 Å images as a stepping-stone. If successful, it will help solar physicists better monitor the activity on the Sun's far side, and better model the solar wind and magnetic field in the corona.

Finally, it is worthwhile pointing out that the availability of our new time–distance helioseismic far-side imaging method complements the existing helioseismic holography method. A combination of the results from both methods will substantially boost the confidence of imaging the Sun's far-side ARs, and therefore provide more reliable far-side information to the solar physics community.

This work utilizes Dopplergrams and magnetograms observed by *SDO/HMI*, and 304 Å observations by *SDO/AIA* and both *STEREO/EUVI* instruments. The helioseismic holography far-side images are routinely produced and distributed by *SDO/JSOC*. Both *SDO* and *STEREO* are NASA missions. We thank Drs. J. Qiu and P. Liewer for providing us the composite 304 Å maps made from *SDO/AIA* and *STEREO/EUVI* observations. This work is partly supported by the NOAA grants WC-133R-16-CN-0116 and NA18NWS4680082.

## REFERENCES

- Arge, C. N., Henney, C. J., Gonzalez Hernandez, I., et al. 2013, AIP Conf. Proc., 1539, 11
- Arge, C. N., Henney, C. J., Koller, J. et al. 2010, AIP Conf. Proc., 1216, 343
- Braun, D. C., & Lindsey, C. 2001, ApJ, 560, L189
- Chen, R., & Zhao, J. 2018, ApJ, 853, 161
- Duvall, T. L., Jr., Jefferies, S. M., Harvey, J. W., & Pomerantz, M. A. 1993, Nature, 362, 430
- Duvall, T. L., Jr., Kosovichev, A. G., & Scherrer, P. H. 2000, Bulletin Am. Astron. Soc., 32, 837
- González Hernández, I., Hill, F., & Lindsey, C. 2007, ApJ, 669, 1382
- Hartlep, T., Zhao, J., Mansour, N. N., & Kosovichev, A. G. 2008, ApJ, 689, 1373



- Harvey, J. W., Hill, F., Hubbard, R. P., et al. 1996, *Science*, 272, 1284
- Henney, C. J., Hock, R. A., Schooley, A. K., Toussaint, W. A., White, S. M., & Arge, C. N. 2015, *Space Weather*, 13, 141
- Howard, R. A., Moses, J. D., Vourlidas, A., et al 2008, *Space Sci. Rev.*, 136, 67
- Ilonidis, S., Zhao, J., & Hartlep, T. 2009, *Sol. Phys.*, 258, 181
- Kosovichev, A. G., Duvall, T. L., Jr., & Scherrer, P. H. 2000, *Sol. Phys.*, 192, 159
- Kosovichev, A. G., Schou, J., Scherrer, P. H., et al. 1997, *Sol. Phys.*, 170, 43
- Larson, T. P., & Schou, J. 2018, *Sol. Phys.*, 293, 29
- Larson, T. P., & Schou, J. 2018, *Sol. Phys.*, 290, 3221
- Liewer, P. C., González Hernández, I., Hall, J. R., Lindsey, C., & Lin, X. 2014, *Sol. Phys.*, 289, 3617
- Liewer, P. C., González Hernández, I., Hall, J. R., Thompson, W. T., & Misrak, A. 2012, *Sol. Phys.*, 281, 3
- Liewer, P. C., Qiu, J., & Lindsey, C. 2017, *Sol. Phys.*, 292, 146
- Lindsey, C., & Braun, D. C. 2000a, *Science*, 287, 1799
- Lindsey, C., & Braun, D. C. 2000b, *Sol. Phys.*, 192, 261
- Lindsey, C., & Braun, D. C. 2017, *Space Weather*, 15, 761
- Scherrer, P. H., Bogart, R. S., Bush, R. I., et al. 1995, *Sol. Phys.*, 162, 129
- Scherrer, P. H., Schou, J., Bush, R. I., et al. 2012, *Sol. Phys.*, 275, 207
- Schou, J., Scherrer, P. H., Bush, R. I., et al. 2012, *Sol. Phys.*, 275, 229
- Schrijver, C. J., & DeRosa, M. L. 2003, *Sol. Phys.*, 212, 165
- Ugarte-Urra, I., Upton, L., Warren, H. P., & Hathaway, D. H. 2015, *ApJ*, 815, 90
- Upton, L., & Hathaway, D. H. 2014, *ApJ*, 780, 5
- Zhao, J. 2007, *ApJ*, 664, L139
- Zhao, J., Nagashima, K., Bogart, R. S., Kosovichev, A. G., & Duvall, T. L., Jr. 2012, *ApJ*, 749, L5

